IOP Publishing and International Atomic Energy Agency Nuclear Fusion
Nucl. Fusion **47** (2007) 612–625 doi:10.1088/0029-5515/47/7/012

Theory and fluid simulations of boundary-plasma fluctuations

R.H. Cohen[1], B. LaBombard[2], D.D. Ryutov[1], J. L. Terry[2], M.V. Umansky[1], X.Q. Xu[1] and S. Zweben[3]

[1] Lawrence Livermore National Laboratory, Livermore, CA 94551, USA
[2] Massachusetts Institute of Technology, Cambridge, MA 02139, USA
[3] Princeton Plasma Physics Laboratory, Princeton, NJ 08540, USA

E-mail: rcohen@llnl.gov

Received 10 January 2007, accepted for publication 16 April 2007
Published 26 June 2007
Online at stacks.iop.org/NF/47/612

Abstract
Theoretical and computational investigations of boundary-plasma microturbulence which take into account important effects of the geometry of diverted tokamaks—in particular, the effect of X-point magnetic shear and the termination of field lines on divertor plates—are presented. We first generalize our previous 'heuristic boundary condition' which describes, in a lumped model, the closure of currents in the vicinity of the X-point region to encompass three current-closure mechanisms. We then use this boundary condition to derive the dispersion relation for low-beta flute-like modes in the divertor-leg region under the combined drives of curvature, sheath impedance and divertor tilt effects. The results indicate the possibility of strongly growing instabilities, driven by sheath boundary conditions, and localized in either the private or common flux region of the divertor leg depending on the radial tilt of divertor plates. We revisit the issue of X-point effects on blobs, examining the transition from blobs terminated by X-point shear to blobs that extend over both the main SOL and divertor legs. We find that, for a main-SOL blob, this transition occurs without a free-acceleration period as previously thought, with X-point termination conditions applying until the blob has expanded to reach the divertor plate. We also derive propagation speeds for divertor-leg blobs. Finally, we present fluid simulations of the C-Mod tokamak from the BOUT edge fluid turbulence code, which show main-SOL blob structures with similar spatial characteristics to those observed in the experiment, and also simulations which illustrate the possibility of fluctuations confined to divertor legs.

PACS numbers: 52.35.Kt, 52.30.Ex, 52.35.Mw, 52.65.-y, 52.40.Kh

(Some figures in this article are in colour only in the electronic version)

1. Introduction

Turbulent transport in the boundary plasma of tokamaks plays an essential role in establishing the boundary conditions for core-plasma transport and in establishing the pattern of power and particle loss to bounding material surfaces. While such transport has been the subject of theoretical, computational and analytic studies for many years, the description of the turbulence has been heavily shaped by two major developments: the recognition of the role of magnetic shear in the vicinity of the separatrix X-point and the emergence of the importance of large-amplitude intermittent structures or 'blobs'.

X-point magnetic shear squeezes magnetic flux tubes, mixing poloidal/toroidal and radial potential variations, thereby raising the effective radial mode number of fluctuations passing near the X-point [1]. The radial wavelength of moderate-toroidal-mode-number perturbations can shrink to less than a gyroradius on passing the X-point region. Various mechanisms—resistive current flow [2], polarization [3–5] and viscosity [6] can lead to current closure in this region, thereby terminating fluctuations present on one side or the other of the X-point, and isolating instabilities in the main SOL from those in the divertor leg. This current closure can be approximated as a lumped boundary condition (BC); this was done for resistive closure in [2], and for polarization in [3–5]. The effective boundary condition can then be used to analyse the effect of X-point shear on instabilities. This was done for curvature-driven modes in the main SOL [7] and for sheath-driven modes in the divertor leg [2].

A number of experiments (e.g. [8–11]) have observed large-amplitude, intermittent, strongly elongated (along the magnetic field) structures or 'blobs'. They are of considerable importance, since they propagate radially and can be a significant transport mechanism to the main chamber walls. These can be viewed as a nonlinear state of instabilities in

the SOL. A simple model was proposed in [13]; more recent treatments have introduced the braking effect of contact with external walls [12, 14] and more quantitative analyses based on the vorticity equation [14, 15].

In the past few years the interaction of the above phenomena has come under investigation: it has been recognized that blobs (like lower-amplitude fluctuations in the edge) can be strongly impacted by the presence of X-point shear, and the effects can be analysed using the 'heuristic boundary condition' described above. [12] derived the terminal velocity of an isolated blob in the main scrape-off layer contact with the X-point region. Recently we pointed out [16, 17] a number of further consequences of X-points and wall contact (or lack thereof) for blob dynamics.

In the present paper we extend the above lines of investigation in several ways. First, we note that the X-point current-closure mechanisms can be combined to a generalized heuristic boundary condition (section 2). We then apply (section 3) the heuristic boundary condition to the analysis of low-β, flute-like, divertor-leg instabilities, under the combined influence of curvature, sheath impedance and radial tilt of divertor plates. In section 4 we gather our previously derived results on the effect of X-point effects on blob propagation and examine the reconnection of a main-SOL blob to the divertor plate as it radially propagates. Also in this section we derive results for the propagation of blobs in divertor legs. Section 5 is devoted to numerical simulation of the above phenomena using the BOUT two-fluid code: main-SOL blobby structures and comparisons with experimental data for the C-MOD tokamak, and simulations indicating the presence of fluctuations in divertor legs uncorrelated with fluctuations in the main SOL. Section 6 is a discussion and summary of the results.

2. X-Point boundary conditions

As mentioned in the introduction, in a number of cases the magnetic shearing of perturbations near the X-point is so strong that it causes a complete decoupling of perturbations at two sides of the X-point. In particular, perturbations in the common flux region of the divertor get decoupled from perturbations in the main SOL, and perturbations in the outer private-flux region in divertor are decoupled from perturbations in the inner region. What happens to perturbations in the transition zone is that the cross-field current becomes non-negligible because of a rapid increase in a perpendicular wavenumber along the field line and the corresponding increase in a cross-field current. The cross-field wavenumber grows, roughly, as $\exp(s/L^*)$ [1], with s being the distance along the field line and L^* being some characteristic length determined by the details of the divertor design and being of order of a few meters for most of the medium-size tokamaks [18]. So, a potential perturbation of the form $\exp(\mathrm{i}\mathbf{k}_\perp \cdot \mathbf{r})$ imposed on the one side of the X-point decays when one moves into the X-point region because of the finite parallel plasma resistance. The situation here is similar to that of the 'leaky circuit,' where the voltage applied between two conductors decreases with the distance from the terminal if there is a current leak from one conductor to another.

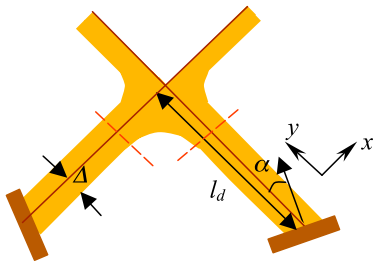

Figure 1. Schematic of the divertor region. Dashed lines represent the 'control planes' for divertor-leg instabilities near the separatrix. The major axis is to the left.

As a rough way to describe this situation, one can impose a resistive boundary condition at a 'control surface' situated at some distance from the X-point. In particular, when one deals with instabilities in the private-flux region, the location of the control surfaces for the outer and inner legs are shown in figure 1. The exact location of these surfaces is not very important if the divertor legs are long enough, so that the SOL width at the divertor plate is much less than the distance from the divertor plate to the X-point. The structure of the boundary condition at this surface is:

$$j_\parallel = \Sigma \delta\phi, \tag{1}$$

where Σ is some coefficient that, generally speaking, depends on the wavenumber and the frequency of perturbations. The form for σ depends on the assumption of the mechanism leading to the cross-field 'leak.'

In [2] it was noted that, when the perpendicular wavenumber of perturbations exceeds ρ_i^{-1}, a cross-field conductivity by electrons becomes possible. This leads to the BC of the form

$$j_\parallel = \sigma_\mathrm{H} k_\perp \delta\phi, \qquad \sigma_\mathrm{H} = \omega_\mathrm{pe}^2/4\pi\omega_\mathrm{ce}, \tag{2}$$

where $k_\perp = |\mathbf{k}_\perp|$. The parameter σ_H has the dimension of electrical conductivity and was called in [2] a 'heuristic conductivity.'

In [6], a closure mechanism associated with the cross-field ion shear viscosity was considered. It leads to the following BC:

$$j_\parallel = \sigma_\mathrm{H} k_\perp \delta\phi \left(\frac{m_\mathrm{i}}{m_\mathrm{e}}\right)^{1/4} (k_\perp \rho_\mathrm{i})^{1/2}. \tag{3}$$

(We find it convenient to express the BC in terms of the heuristic conductivity, which allows easy comparison between various models.)

In [3–5], closure by the ion polarization current was considered. This yields the following BC:

$$j_\parallel = \sigma_\mathrm{H} k_\perp \delta\phi \left(\frac{m_\mathrm{i}}{m_\mathrm{e}} \frac{|\omega|}{\nu_\mathrm{ei}}\right)^{1/2}. \tag{4}$$

The last two mechanisms are based on the assumption that the cross-field length-scale of the perturbation in the sheared region remains greater than the ion gyroradius all over the zone where the closure of the currents occurs. If, formally,

the closure does not occur up to the point where the length-scale becomes less than ρ_i , then the mechanism described by equation (2) takes over.

In the derivation of boundary conditions (2)–(4) in [2–6], a WKB-type analysis of the modes above the control surface (for the geometry of figure 1) was used. In this analysis the exact location of the control surface is not important, provided the divertor leg is long enough. This is due to the fact that the cross-field current leak becomes significant only in the zone near the X-point where a strong squeezing of the flux tubes begins. In the vicinity of the control surface the parallel electric field is small and the exact position of this surface has a very weak effect on the evaluation of the parameter Σ in equation (1).

The BC for a specific set of parameters is determined by the mechanism that yields the highest current. One can qualitatively take this circumstance into account by introducing a 'generalized boundary condition' that can be obtained simply by summing up equations (2)–(4). The result is

$$j_\parallel = \sigma_H k_\perp \delta\phi \left[1 + \alpha_1(k_\perp) \left(\frac{m_i}{m_e}\right)^{1/4} (k_\perp \rho_i)^{1/2} + \alpha_2(k_\perp) \left(\frac{m_i}{m_e}\frac{|\omega|}{\nu_{ei}}\right)^{1/2} \right]. \quad (5)$$

The coefficients $\alpha_1, \alpha_2 < 1$ account for the aforementioned possibility that the length-scale reaches the ion gyroradius before the substantial shortening of the current by a particular mechanism occurs. The values of these coefficients depend on the specifics of the divertor geometry. For the plasma parameters chosen in section 3, 4 all the mechanisms yield the same contribution to $j_\parallel$, to within a factor of 2–3. In order not to overload our largely conceptual analysis by the unnecessary details we use in section 3 and 4 simply the boundary condition (5) with the term in square brackets replaced by a constant G,

$$j_\parallel = G\sigma_h |\boldsymbol{k}_\perp| \delta\phi, \quad (6)$$

with $G \sim 1$; this is of course just our heuristic boundary condition (2) with an extra multiplicative factor G. This discussion closely follows the discussion in appendix C of [5]. A new element is the inclusion of the viscous term (3).

When boundary condition (5) is applied to the perturbations existing between the divertor plate and the control surface, the exact location of the latter is, again, unimportant: moving the control surface up or down by the distance $\delta\ell_d$ small compared with the length ℓ_d of the divertor leg causes the appearance of corrections of the order of $\delta\ell_d/\ell_d$ in the eigenfrequencies. For this approach to be valid, the divertor legs need to be long enough, exceeding, roughly, $(a\Delta_0)^{1/2}$ where a is the minor radius and Δ_0 is the SOL width in the equatorial plane [16].

3. Divertor-leg and private-flux instabilities

The plasma in the divertor is in direct contact with the divertor plates and, therefore, may be strongly affected by the sheath boundary conditions. In the private-flux region there is obviously no connection with the main SOL along magnetic-field lines. In the common flux region the connection is present but may be strongly reduced by the shear near the X-point. As noted in [2, 16, 19] these features can be used to reduce the divertor heat load by exploiting various instabilities specific to the divertor plasma so that the plasma cross-field diffusion in the divertor legs would be maximized and lead to a broadening of the wetted area. On the other hand, the possibility of confining these instabilities within the divertor leg, without inducing additional transport in the main SOL, would eliminate any adverse effect of these instabilities on the pedestal formation and bulk plasma confinement. This approach generally favours divertors with 'long legs' and can therefore improve performance of the X divertor [20].

In this paper we present an analysis of divertor-leg instabilities that consistently includes curvature, X-point shear and sheath BC; we discuss the consequences for instabilities in the private-flux region. We use the generic divertor geometry shown in figure 1. The angle α is considered positive when the tilt of the divertor plate is as shown in figure 1. We assume that the distance ℓ_d from the X-point to the divertor plate is ~ 20 cm, toroidal field $B_T \sim 5$ T, poloidal field $B_P \sim 0.3$ electron temperature at the divertor floor $T_e \sim 25$ eV, plasma cross-field length-scale $\Delta \sim 1$ cm in the private-flux region at the divertor plate and density $n \sim 10^{13}\,\mathrm{cm}^{-3}$. These parameters roughly correspond to those of a high-field compact tokamak like C-Mod, although they do not reflect details of any particular tokamak. We assume also that the plasma fills the whole flux tube connecting the inner end outer strike points, neglecting variation of the parameters along the flux tube.

We consider unstable modes satisfying $\Delta^{-1} < k_\perp < \rho_i^{-1}$, where $\rho_i = c_s/\omega_{ci}$ with $c_s = (2T_e/m)^{1/2}$. The modes are flute-like, with $k_\parallel \ll k_\perp$. For the set of parameters mentioned above, $\rho_i \sim 0.02$ cm (deuterium). An important factor is the squeezing of the flux tubes on their way from one strike point to the other, caused by strong shear near the X-point [1,18]. A flux tube that is circular at one strike point and centred a distance Δ_0 from the separatrix ends up having a highly stretched elliptical cross section, with ellipticity $E \approx (\ell_d/\Delta_0)^2$. Hence a perturbation with wavenumber $k_\perp$ at the outer strike point has a scale length $k_\perp^{-1}E^{-1/2} \sim k_\perp^{-1}\Delta_0/\ell_d$ near the inner strike point. If this scale-length becomes less than ρ_i, the perturbation is 'dissolved' in the ambient plasma. In this case perturbations in the two legs are disconnected and the effect of the X-point shear can be approximated by the 'heuristic boundary condition' (6) on control planes situated somewhat below the X-point (dashed lines in figure 1). Conversely, if $\Delta_0/k_\perp\ell_d > \rho_i$, the perturbation may connect the two strike points. Estimating $\Delta_0 \approx \Delta/2$, one finds that the disconnection occurs for perturbations with $k_\perp\rho_i > \Delta/2\ell_d \sim 1/40$, i.e. even for perturbations with the cross-field length-scale approaching the plasma thickness Δ. Therefore, we consider only disconnected perturbations. (We will return to the process of disconnection in connection with our discussion of blobs in the next section.)

We apply a sheath BC at the divertor plate, with the effects of tilt ($\sin\alpha \neq 0$) and plasma drifts included, and the heuristic BC at the control surface. We assume $T_e^{-1}\nabla_\perp T_e \gg n^{-1}\nabla_\perp n$ and neglect the latter. The general dispersion relation accounting for possible finite-beta effects is derived in the appendix. In the case of the plasma parameters mentioned above the plasma beta is quite small and, as we will check shortly, the perturbations have a pure flute nature. The

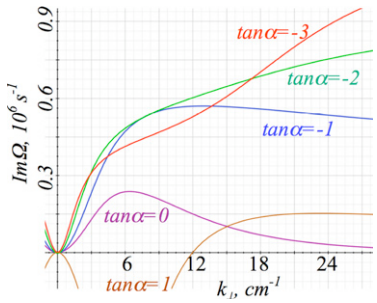

Figure 2. Growth rate versus wavenumber for the private-flux region in the outer leg, for $L_\parallel = 3\,\mathrm{m}$, $R = 0.7\,\mathrm{m}$, $G = 2$, and other parameters as indicated in the text. At zero tilt, there is only a weak instability. Negative tilt makes the plasma strongly unstable.

dispersion relation then looks as follows (cf. equations (A.39) and (A.40)):

$$\Omega^2 + \Omega(\mathrm{i}\Omega_1 + \Omega_2 + \mathrm{i}\Omega_3) - \mathrm{i}\Gamma_1^2 - \Gamma_2^2 - \Gamma_3^2 = 0 \qquad (7)$$

with

$$\Omega_1 = \frac{\omega_{\mathrm{ci}}^2 m_\mathrm{i} c_\mathrm{s}}{L_\parallel k_y^2 T_\mathrm{e}}, \qquad \Omega_2 = \frac{\omega_{\mathrm{ci}}}{k_y L_\parallel}\frac{B_\mathrm{T}}{B_\mathrm{P}}\tan\alpha,$$

$$\Omega_3 = \frac{B_\mathrm{T}\omega_{\mathrm{ci}} G}{B_\mathrm{P}|k_y|L_\parallel},$$

$$\Gamma_1^2 = \frac{\hat{\Lambda}\omega_{\mathrm{ci}} c_\mathrm{s}}{k_y L_\parallel \Delta}, \qquad \Gamma_2^2 = \pm\frac{T_\mathrm{e}}{m_\mathrm{i} L_\parallel \Delta}\tan\alpha,$$

$$\Gamma_3^2 = \pm\frac{2^{1/2} T_\mathrm{e} B_\mathrm{T}}{m_\mathrm{i} R \Delta B_\mathrm{P}},$$

with $L_\parallel$ the distance along a field line from the divertor plate to the control surface and with the constant $\hat{\Lambda} =\sim (1/2)(1+\Lambda) \sim 4$. Here G is the adjustment factor of order one that enters the heuristic boundary condition (6), $\Lambda = \ln(2\pi)^{-1/2}\times$ the ratio of the electron to ion thermal speed, and R is evaluated at the strike point. The 'plus' ('minus') sign corresponds to the private-flux region in the outer (inner) leg.

The first term in the left-hand side (lhs) of equation (7) describes plasma inertia. The last term describes curvature stabilization (destabilization) of perturbations: in the private-flux region, for the outer leg, it is stabilizing, whereas for the inner leg it is de-stabilizing. The second to the last term describes the stabilizing/destabilizing effect the divertor-plate tilt. In order to have stronger turbulent broadening of the private-flux region it is desirable to have $\alpha < 0 (> 0)$ in the outer (inner) leg. The Ω_3 term describes the effect of the X-point-shear boundary condition. The rest of the terms come from the sheath boundary condition (see appendix).

The growth rate determined from equation (7) is shown in figure 2. One sees that the tilt of the divertor plate has a strong effect on the instability. To enhance the instability in the outer (inner) private-flux region, the tilt has to be negative (positive). As shown in [2], the real part of the frequency at moderate k is of the order of the growth rate, i.e. $f = \mathrm{Re}\Omega/2\pi \sim \mathrm{Im}\Omega/2\pi \sim 100\,\mathrm{kHz}$. The diffusion coefficient evaluated by a mixing length estimate is quite high, approaching $1.5\,\mathrm{m}^2\,\mathrm{s}^{-1}$ (i.e. significantly higher than Bohm).

Consider now the applicability conditions as described by equations (A.41)–(A.43). Taking as representative values $k_y = 8\,\mathrm{cm}^{-2}$ and $|\Omega| = 5\times10^5\,\mathrm{s}^{-1}$ (figure 2) and evaluating the magnetic diffusivity for $T_\mathrm{e} = 25\,\mathrm{eV}$ as $D_m \sim 3\times10^4\,\mathrm{cm}^2\,\mathrm{s}^{-1}$, one finds that condition (A.42) is satisfied. Therefore, the validity of the pure flute approximation is determined by condition (A.43). Using equation (A.25) and taking $L_\parallel = 3\,\mathrm{m}$ (as in figure 2), one finds that $\ell_\mathrm{d} = 20\,\mathrm{cm}$. The Alfvèn velocity for a deuterium plasma with $n = 10^{13}\,\mathrm{cm}^{-3}$ in a magnetic field of 5 T is $2.5\times10^9\,\mathrm{cm\,s}^{-1}$. Therefore, the lhs of equation (A.43) is ∼0.1, signifying the validity of the flute approximation.

At the nonlinear stage of the instability, one can expect formation of blobs [13] moving away from the separatrix, deeper into the private-flux region. This is discussed in the next section.

4. Blobs

In the past few years it has been recognized that blobs (like lower-amplitude fluctuations in the edge) can be strongly impacted by the presence of X-point shear and the effects can be analysed using the 'heuristic boundary condition' described in section 2. Reference [12] derived the terminal velocity of an isolated blob in contact with the X-point region. Recently we pointed out [16, 17] a number of further consequences of X-points and wall contact (or lack thereof) for blob dynamics. Here we collect these results, and then examine two aspects that were not explicitly treated previously: the process by which a blob loses contact with the X-point region, and the condition for resistive ballooning isolating a blob from the end walls. We then consider the implications for blob propagation in C-Mod, where some rather detailed studies of blob propagation have been performed. Finally we discuss properties of blobs that follow from the divertor-leg instabilities discussed in the preceding section.

The salient results from [16, 17] are:

(1) The X-points decouple blobs and blob dynamics in the main SOL and in the divertor legs. Blobs born close to the separatrix in either the main SOL or the divertor leg will be confined to that region until they have propagated out far enough that the X-point shearing is sufficiently weak. The terminal velocity of a blob confined to the main-SOL region is of order

$$\dot{R}_x \sim v_\mathrm{ti} L_x \rho / G R a \qquad (8)$$

where L_x is the field line connection length (half the field line length) to the X-point region, a is the blob radius, ρ is the gyroradius and G is the order-unity phenomenological constant in the X-point heuristic boundary condition.

(2) Divertor leg instabilities, such as discussed in section 3, can grow into blobs localized to the divertor legs. These move slower than main-SOL-localized blobs because of contact with the divertor (see discussion below).

(3) If a blob is found close to the separatrix which appears to extend all the way from the main SOL to the divertor floor, this must be considered as a coincidental alignment of a main-SOL and divertor-leg blob; the two will each propagate at their own rate.

(4) when a blob has propagated sufficiently far from the separatrix that X-point shear is insufficient to bring the blob thickness down to the gyroradius, it ceases to be

confined poloidally to one side or the other of the X-point region. (We examine below just where and how this occurs). We had argued previously that the blob would then enter a period of acceleration while simultaneously expanding along the magnetic field at thermal speed until a material surface is reached, but the discussion below indicates this period is of zero length.

(5) A blob in contact with a material surface, and for which the pressure or density distribution within the blob cross section is non-symmetric, experiences a conducting-wall drive in addition to the better-known curvature drive. These blobs are the nonlinear limit of the conducting-wall temperature-gradient modes described in [21, 22]. The terminal velocity in the case where this drive dominates over curvature drive (valid for $\Lambda a R F_a/\rho_i L_c > 1$, where $\Lambda = \hat{\Lambda} - 1/2 \sim 3$, L_c is the connection length ($\sim$ half the field line length) and $F_a < 1$ is a measure of the degree of asymmetry of the pressure and density distributions) is [17]

$$\dot{R}_{cw} \sim F_a \Lambda c T_{e,wall}/eBa \tag{9}$$

(neglecting modifications, analogous to those discussed in the preceding section, when there is a significant tilt of the bounding surface); in the opposite limit, it is

$$\dot{R}_\kappa \sim (cT_e/eBa)(\rho_s L_c/Ra)(1 + T_i/T_e). \tag{10}$$

The question of how a blob, initially confined to the main SOL plasma, re-establishes connection through the divertor leg to the divertor plates, and the associated question of how far from the separatrix the X-point is effective in isolating a blob has not been explicitly dealt with in the previous literature. An estimate for this 'connection distance' Δ_c proceeds as follows. We refer in this section to coordinates as defined in figure 1, with the origin of x, y taken at the X-point. We note that, with this choice, $x > |y|$ denotes positions along a (hyperbolic, $xy = \text{const}$) field line in the main SOL, and $x < |y|$ denotes positions in the divertor leg. We also note that, in the former case, x is an approximate measure of the poloidal distance (in the main SOL) from the vicinity of the X-point while in the latter case $|y|$ plays the same role in the divertor leg. Similarly, y measures the distance normal to the flux surface from the point to the separatrix in the main SOL while x plays the same role in the divertor leg. That is, the approximate association of x and y with distances within and across flux surfaces reverses between the main SOL and the divertor leg.

As noted in [1] and in section 2, a flux tube that is circular far above the X-point (at position x_0, y_0), with radius a, is elliptically distorted to have a thickness (minor radius) $\delta R \approx a y_0/|y_c|$ at the position x_c, y_c (where $x_c = x_0 y_0/y_c$). So a flux tube will be distorted to have a specified thickness δR at the position where $|y_c| = a y_0/\delta R$, which increases linearly with the distance y_0 from the separatrix. But interestingly, the value of x at this position does not change with y_0; it is just $x_c = x_0 \delta R/a$. Putting together this result with our observations about the roles of x and y as measures of poloidal and cross-flux-surface distance above and below the X-point, and defining the 'control surface' discussed in the preceding sections as the point where δR has a fixed value ($\sim \rho_i$), we can now infer how the poloidal position of the control surface moves as a blob propagates radially. We see that as y_0 is increased, the control surface is almost stationary at a distance $\sim x_c$ up the main-SOL leg until $|y_c|$ becomes comparable with x_c, which, from the above estimates, occurs at a distance from the separatrix $y_0 \sim x_0(\rho/a)^2$; once $|y_c|$ exceeds x_c the control surface advances down the divertor leg approximately linearly with increasing y_0. This estimate continues to apply so long as the poloidal field is approximately quadrupolar, i.e. up to $|y_c| \sim r$, the tokamak minor radius. The moving control surface approximately determines the poloidal extent of the radially propagating blob. For purposes of obtaining numerical estimates, one can take $x_0 \sim r$ in the above expressions.

One might be concerned that, once the control surface for a main-SOL blob is in the divertor leg, it might recede towards the divertor faster than the material in the blob can catch up. However, within the context of the quadrupolar model, the toroidal distance between the position where a flux tube is circular with a specified radius r_0 and the position where it is elliptical with minor radius ρ_i is independent of the distance from the separatrix, and is just $\Delta z = (B_T/B'_P)\ln(r_0/\rho_i)$, where B_T is the toroidal field strength and B'_P is the (constant) derivative of the poloidal magnetic field with respect to distance from the X-point. Hence as a blob propagates outwards, this poloidal distance does not change. As a first approximation, one might argue that to leading order in B_P/B_T, purely transverse displacement of a flux tube segment consists of purely poloidal motion and so preserves the toroidal length; hence mass initially at the control surface would exactly keep up with it, without the need for any flow along field lines. But this is not quite correct; transverse displacement necessarily involves some toroidal motion as well, which means that a flux tube segment whose end is initially a gyroradius thick is no longer a gyroradius thick after displacement. Some parallel (to $\boldsymbol{B}$) mass flow is required for mass to stay with the moving control surface as a blob propagates.

To estimate the effect, consider again a flux tube with circular cross section of radius a_0 at position x_0, y_0 (where x_0 is the tokamak minor radius and $-y_0$ is the SOL width). This flux tube is squeezed to a radial extent $\delta x \sim \rho_i$ at position $y_f \approx y_0(a_0/\rho_i)$, $x_f = x_0 y_0/y_f$. (Initially x_f, $y_f = x_c$, y_c, the position of the control surface). Note that the flux tube is extended in the poloidal (y) direction here, $\delta y \sim a_0^2/\rho_i$. We consider a purely transverse displacement of the flux tube which is purely in the poloidal plane at x_0, y_0; for a radial displacement ξ_{0y}, there is a poloidal displacement $\xi_{0x} \sim -\xi_{0y} B_y/B_x = \xi_{0y} y_0/x_0$, and by construction zero toroidal displacement. We look for the point on the displaced field line which is reached by a purely transverse (to $\boldsymbol{B}$) displacement from the point x_f, y_f, z_f, That is, $\boldsymbol{\xi}_f \cdot \boldsymbol{B} = 0$, from which it follows that $\xi_{fz} = (B'_P/B_T)(x_f \xi_{fx} - y_f \xi_{fy})$. Just as the shear results in the flux tube being elongated in the y direction, the displacement ξ_{yf} is enhanced over the main-SOL displacement ξ_{y0} by the same factor $\sim a_0/\rho_i$. Hence we find, approximately, $\xi_{fz} \sim -\xi_{y0} B'_P y_F^2/B_T y_0 \sim \xi_{y0}(B_P/B_T)a/\rho$. Hence, as a blob moves outwards with velocity $\dot{R}$, there must be a parallel flow (approximately equal to the toroidal flow) of magnitude $v_\parallel \sim \dot{R}(B_P/B_T)(a/\rho_i)$ in order to preserve Δz and so stay in contact with the receding control surface. For typical parameters $(B_P/B_T)(a/\rho_i) \sim 1$; the required parallel flow velocity is of the same order as the blob radial expansion velocity, which is typically well below the sound speed. So, the

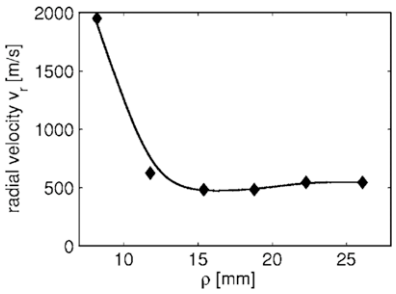

Figure 3. Blob propagation speed in C-Mod, from [9].

blob can keep up; the X-point boundary condition will continue to apply until the control surface reaches the divertor plate. The limit of applicability of the X-point boundary condition is then simply given by $\Delta_c \approx \rho\ell_d/a$. A blob propagating past this point will transition from a terminal velocity set by X-point shear to a terminal velocity set by contact with the divertor plate.

Now we consider the effects of resistive ballooning. In conjunction with blob physics, various aspects of this issue have been discussed in [4,5,17]. For our purpose the analysis presented in [17] is most convenient as it explicitly describes the dynamical evolution of the central line of the isolated plasma filament (the isolated blob). Equations (42) and (43) of [17] are coupled partial differential equations for the evolution of the normal and geodesic component of displacement for a blob derived in the approximation of resistive MHD, and are of the form

$$C_1\ddot{\xi}_g + \frac{B^2}{c^2}\frac{\partial}{\partial s}\left[C_{gg}\left(\frac{B}{B_P}\xi_g\right) + C_{gn}\left(B_P R\xi_n\right)\right] + S_g = 0 \quad (11)$$

and

$$C_1\ddot{\xi}_n + \frac{B^2}{c^2}\frac{\partial}{\partial s}\left[C_{nn}\left(\frac{B}{B_P}\xi_n\right) + C_{ng}\left(B_P R\xi_g\right)\right] + S_n = 0, \quad (12)$$

where $C_1 = \int \rho \mathrm{d}S$, $C_{jg} = \left(\int \sigma \mathrm{d}S\right) D_{jg} B_P/B^2$, $C_{jn} = \left(\int \sigma \mathrm{d}S\right) D_{nj}/B B_P R$, and $S_j = [2(\nabla B)_j/B]\int p \mathrm{d}S$ for $j = g, n$, $\int \mathrm{d}S$ denotes an integral over the cross section of the blob, $D_{ij} = \langle x_i x_j\rangle - \langle x_i\rangle\langle x_j\rangle$, σ is the electrical conductivity, and the $\langle\ \rangle$ denotes a σ-weighted average over the blob cross section. The resistive-ballooning limit prevails when the parallel derivative terms in these equations are negligible compared with the remaining terms, from which we obtain the following criterion:

$$\dot{R} \ll \dot{R}_b = \beta c^2 L_c^2/\pi a^2 \sigma R, \quad (13)$$

where σ is the parallel conductivity. This criterion can also be obtained from analysing equations (8) and (9) of [5].

We now consider application of these considerations to C-Mod. Reference [9] contains a plot of blob velocity versus radius for a representative discharge, reproduced here as figure 3. A detailed analysis of experimental data regarding blobs (including in C-Mod) has been recently published [10]. Our study identifies additional effects, in particular: (1) the conducting-wall drive, associated with temperature and density non-uniformity over the cross section of a blob which has one end is in contact with a conducting surface and (2) the interplay between the poloidal and radial motion of a main-SOL blob as it transitions from being terminated by X-pont shear to making contact with divertor plates. A striking feature of figure 3 is that, apart from the large velocity shown at the smallest radius (which the authors regard as an instrumental artefact), the velocity is nearly constant, and does not show much structure. One is then led to ask how to reconcile this with theoretical predictions of blob speeds that depend on what surfaces the blob contacts and whether it passes close to the X-point. Appeals to ballooning do not help: blobs in C-Mod are observed to have radii $\sim$1 cm (see, e.g. figure 9 of [9]); hence taking $B = 5\,\mathrm{T}$, $R = 0.9\,\mathrm{m}$, the ballooning criterion, equation (13), becomes $\dot{R} \ll \dot{R}_b \sim 94\,\mathrm{m\,s^{-1}} \times (n/5\times10^{13}\,\mathrm{cm^{-3}})(L_c/5\,\mathrm{m})^2(1\,\mathrm{cm}/a)^2(T/20\,\mathrm{ev})^{-1/2}$, which, for the observed blob velocity from figure 3 and typical C-Mod parameters, is not satisfied except possibly very close to the separatrix where the field lines become very long. So indeed we must consider where blobs end. The criterion that they 'end' at the X-point control surface rather than at the divertor plate, $\Delta < \Delta_c = \rho\ell_d/a$, becomes $\Delta < 0.4\,\mathrm{cm} \times (T_{e,\mathrm{wall}}/10\,\mathrm{eV})(\ell_d/20\,\mathrm{cm})$. (Because of the shape of the C-Mod divertor, ℓ_d varies appreciably.) Thus only the left-most data point in figure 3 is possibly subject to the X-point boundary condition. For all other data points the blobs are in contact with either the horizontal leg of the divertor structure or the antenna limiter. For C-Mod conditions with the asymmetry parameter $F_a \sim 1$, the criterion for dominance of conducting-wall drive for blobs is strongly satisfied; hence for all blobs that end on a wall (limiter or divertor), we estimate

$$\dot{R} = \dot{R}_{cw} \sim 640\,\mathrm{m\,s^{-1}} \times (T_{e,\mathrm{wall}}/10\,\mathrm{eV})(1\,\mathrm{cm}/a)F_a. \quad (14)$$

This is of the right order of magnitude and could plausibly be consistent with a constant blob velocity if the asymmetry parameter F_a compensates for a decrease in blob temperature as it propagates. For a blob that terminates in the X-point shearing region (possibly, marginally, the left-most data point), we obtain $\dot{R} = \dot{R}_x \sim 4400\,\mathrm{m\,s^{-1}} \times (T/20\,\mathrm{eV})(2/G)(1\,\mathrm{cm}/a)$; a blob that just misses termination by X-point shearing would instead terminate on the vertical surface of the C-Mod divertor structure, which would also have an elevated propagation speed because of the tilt of the surface relative to poloidal field lines. The change in velocity between the first and second data points in figure 3 is plausibly the slowing-down of the blob as it transitions from ending in the X-point region or the vertical divertor surface to terminating on the horizontal divertor or limiter surfaces.

We return to the discussion of divertor-leg blobs, noted in section 3. If the electron temperature in the blob is uniform, the drive is associated with the curvature and the tilt of the divertor plates. The contact with the conducting divertor plate partially reduces the polarization field and gives rise to a constant-velocity motion. The X-point 'heuristic boundary condition' turns out to be high resistance compared with the sheath, and so is effectively insulating. This leads to the estimate for the blob velocity, $\dot{R}_{dl} = (\rho_i^2 c_s/a^2)[(L_\parallel/R) \pm (B/B_P)\tan\alpha]$, where + (−) corresponds to the inner(outer) divertor leg in the private-flux region, and opposite for the common flux. If the tilt term dominates over the curvature term by $\mathcal{O}(1)$, blob motion is strong enough to strongly affect transport; the ion parallel transit time is longer than the blob propagation time over the SOL width Δ even for blobs with size Δ for the parameters of section 3. If the broadening is sufficient to

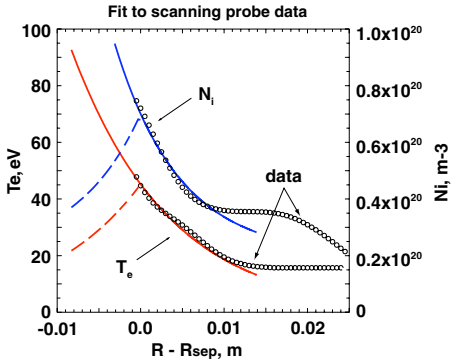

Figure 4. Background profiles used for BOUT simulations of C-Mod. Solid lines are profiles in the edge and main scrape-off layer; dashed lines are profiles in private-flux region. The circles are experimental data points.

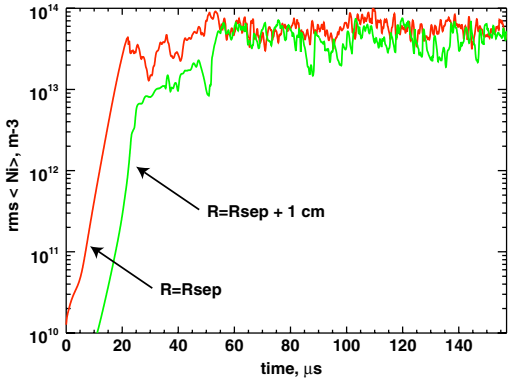

Figure 5. Growth and saturation of fluctuations of C-Mod simulations.

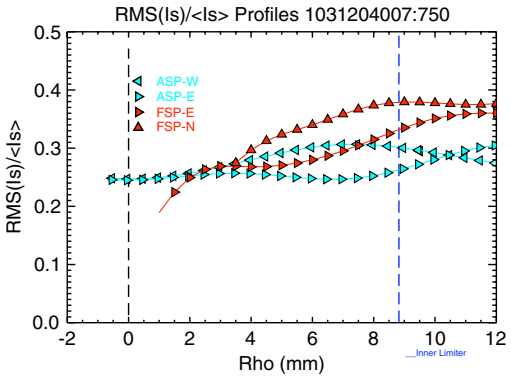

Figure 6. Fluctuations of the saturation current from scanning probe in C-Mod.

result in reconnection of the inner and outer strike points in the private-flux region, and there is enough tilt with favourable signs at both plates, further broadening is possible. Finally, we note a preliminary report of an observation on the MAST spherical tokamak suggestive of the existence of a divertor-leg blob; fast camera observations in visible light during ELM-free periods following an L–H transition appear to show continued presence of field-line-following filaments in the divertor region but an absence of filaments in the main SOL [23].

5. BOUT Simulations

We present in this section simulations of edge turbulence using the BOUT code [24], that illustrate the concepts discussed in the preceding sections. Specifically we address simulations of blobby turbulence in C-Mod, and present simulations showing divertor-leg turbulence uncorrelated with main-SOL turbulence for DIII-D.

The edge plasma in C-Mod is relatively dense ($n_\mathrm{i} \sim 0.5\times10^{20}\,\mathrm{m}^{-3}$) and cold ($T_\mathrm{e} \sim 30\,\mathrm{eV}$), making it a particularly good choice for application of the collisional Braginskii-based plasma model. A particular C-Mod shot 1031204007, $t = 740\,\mathrm{ms}$ is modeled with the magnetic geometry based on an EFIT reconstruction. For the profiles of background plasma density $N_{\mathrm{i}0}$ and temperature $T_{\mathrm{e}0}$ a fit is constructed to match the scanning Langmuir probe measurements at the outer midplane location, with no poloidal variation. In divertor legs the radial profile is taken symmetric with respect to the separatrix, see figure (4). The background ion temperature, $T_{\mathrm{i}0}$, is taken identical to $T_{\mathrm{e}0}$, and no background equilibrium flow and no equilibrium electric potential is used. In the calculation the toroidally average components of fluctuating fields are subtracted out, thus keeping the toroidally average components unchanged.

Two simulation cases are considered, one treating the magnetic equilibrium as a lower single-null (LSN), and the other extending the domain to include the secondary X-point resulting in an unbalanced double-null (UDN). This C-Mod discharge is nominally considered a LSN, and the first simulation is done for that geometry.

As usual, the simulation is initiated with a small seed perturbation, which evolves through linear instability to a saturated turbulent state, see figure (5). The linear growth can be estimated from figure (5) as $\sim$0.25e6 s^{-1}. Comparing that with the linear dispersion relation curves in figure 2 using $k_\perp = 5\,\mathrm{cm}^{-1}$ and $\alpha = 0$ (consistent with BOUT's boundary conditions) one finds excellent agreement with the linear theory.

The saturated amplitudes of calculated N_i fluctuations are quite high: more than 50% at the separatrix and more than 100% further out, see figure (5). That is a factor 2–3 larger than the experimentally measured fluctuations of the ion saturation current normalized to the mean value of the ion saturation current see figure (6), which is taken as an estimate of $\mathrm{RMS}(N_\mathrm{i})/\langle N_\mathrm{i}\rangle$ in the experiment.

The evolution of turbulent plasma is followed for 500 μs, spanning many dozens of eddy turn-over times. The appearance of turbulent eddies is qualitatively similar to that typically observed in the experiment with the fast cameras. To make a quantitative comparison with the experiment a statistical analysis is performed yielding basic parameters such as the auto-correlation time, τ, and auto-correlation lengths in the radial, L_rad,and poloidal, L_pol, directions. The value of L_pol is found to be in the range of typical experimental values, 0.5–1.0 cm, while L_rad is smaller than experimental values 0.5–1.5 cm. However the radial domain size for the LSN case is just 2 cm, constrained by the location of the secondary separatrix, which suggests that the outer boundary condition (zero fluctuation amplitude) may be affecting the solution. This LSN domain limitation is overcome by running the same

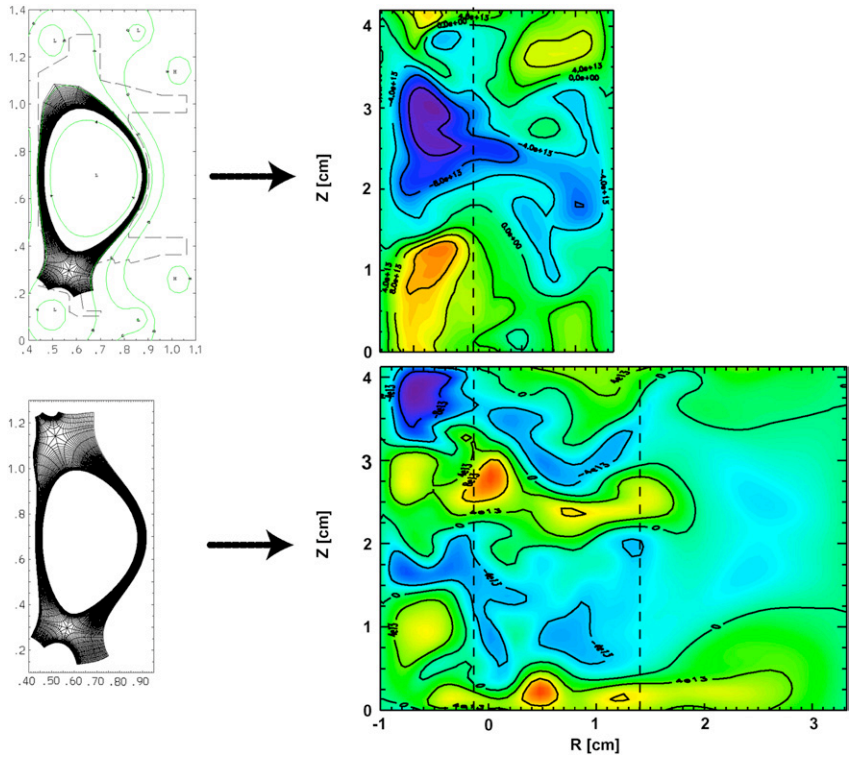

Figure 7. Fluctuations of density at outer midplane for single-null and double-null BOUT runs for C-Mod.

case as a UDN, thereby allowing access to the more distant radial plasma region. Comparison of the two cases is shown in figure (7) where the UDN case yields more radially extended turbulent structures than the LSN case. That is confirmed by figure (8) where $L_{\rm rad}$ and $L_{\rm pol}$ are plotted versus the poloidal and radial coordinates, respectively. The corresponding range of experimental correlations lengths averaged over all radii are shown by the shaded areas. One can see in figure (8) that $L_{\rm pol}$ is quite similar for the two cases, as expected,while $L_{\rm rad}$ is considerably larger for the UDN case. Comparison of the correlation time (to 1/2 of the auto-correlation peak) is less satisfactory. The BOUT values for both cases are about 2 μs, whereas C-Mod measurements indicate a value about 5 times larger. Reasons for this difference are being investigated.

For quantitative assessment of the effects of X-point geometry in these runs we calculate the cross-correlation function for the fluctuating quantities. The cross-correlation function is defined as follows:

$$C(\tilde{\phi},\tilde{\phi}) = \frac{<\tilde{\phi}(r_0,\theta,\zeta+\Delta\zeta,t+\tau)\tilde{\phi}(r_0,\theta_{\rm ref},\zeta,t)>_{\zeta,t}}{<|\tilde{\phi}(r_0,\theta_{\rm ref},\zeta,t)|^2>_{\zeta,t}} \qquad (15)$$

Here r_0 is the radial index of the chosen flux surface, ζ is the toroidal grid index (constant on field lines) and θ is the poloidal index. Also, τ is the time lag, and $\theta_{\rm ref}$ is the reference poloidal index.

In figure (9) we plot the absolute value of the cross-correlation function as a function of the poloidal index (that goes from the inner target plate to the outer one) and the radial coordinate expressed as the radial distance from the separatrix at the outer midplane. The reference location for the cross-correlation function is taken at the outer midplane. One can

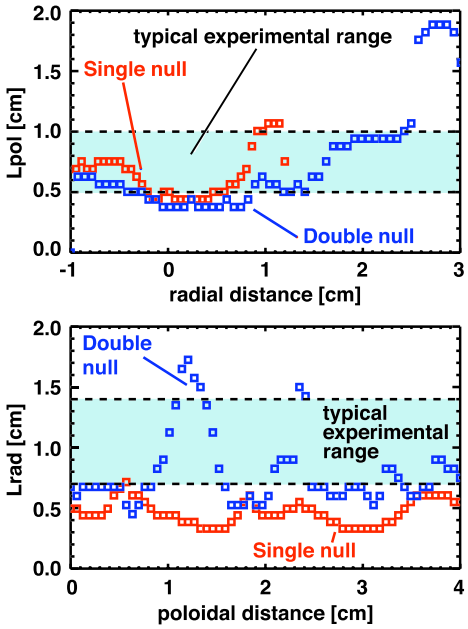

Figure 8. Correlation lengths for fluctuating density at outer midplane for single-null and double-null BOUT runs for C-Mod.

observe in figure (9) that, for small radial distances from the separatrix, the poloidal extent of the correlated perturbations is independent of radial distance, but for larger distances the penetration of perturbations past the lower X-point becomes stronger, as the X-point gets farther away. On the other hand, as the radial coordinate grows the secondary X-point at the top of the plasma becomes closer, and the cutoff of fluctuations near the upper X-point becomes stronger. A plot of the rms

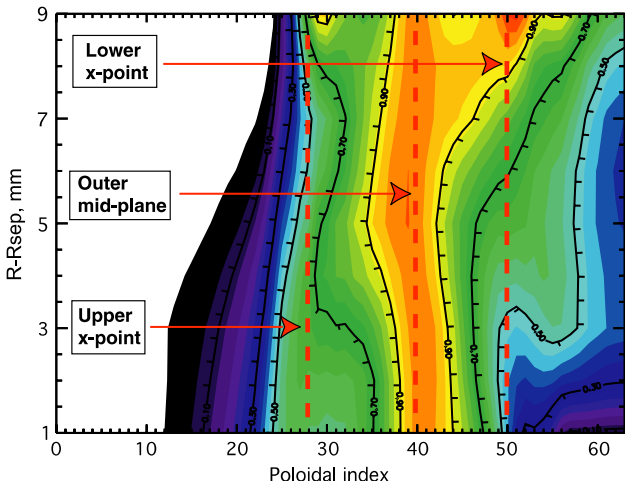

Figure 9. Cross-correlation function for the fluctuating $\tilde{\phi}$ (for $\tau = \Delta\zeta = 0$) as a function of the poloidal index and the radial coordinate for the C-Mod simulation.

density fluctuation shows very little activity in the divertor leg (in contrast to the DIII-D simulations discussed below); hence for this run the poloidal extent of the high correlation region can be taken as an indication of the poloidal extent of the structures. The observed trends—slow evolution of the poloidal extent until the closest approach to the X-point is crossed, followed by more rapid expansion into the divertor leg—are consistent with the theory predictions from section 4.

We can be somewhat more quantitative in our comparisons; from figure (9) we can estimate the rate of increase in the poloidal extent of a blob with increase in radius, from the slope of the level surface of the correlation. The poloidal length corresponding to a unit increase in poloidal index varies (the grid is non-uniform), but is around 1 cm in the divertor leg. From the slope in the figure, we therefore infer that the change in poloidal length of a blob with radial position $\mathrm{d}\ell_\mathrm{p}/\mathrm{d}R \sim 30$. From the discussion in section 4 (the second paragraph following equation (10)), our theory predicts this rate of change to be $\mathrm{d}|y_\mathrm{c}|/\mathrm{d}y_0 = a/\rho$ where a is the blob radius at the midplane. Taking $T = 20\,\mathrm{eV}$ $B = 5\,\mathrm{T}$, and deuterium, and taking as a typical blob radius from the simulation $a \sim 0.5\,\mathrm{cm}$, we obtain a theoretical estimate $\mathrm{d}y_\mathrm{c}/\mathrm{d}y_0 \sim 30$ in agreement with the simulations. (The precision of this agreement we regard as fortuitous, since all of the parameters used for the estimates vary over the domain of the simulation.)

We further consider a comparison of the blob propagation speed from BOUT with the estimates of section 4. By examining successive frames of the simulation from which the upper plot in figure 7 is drawn we can infer propagation speeds in the range of several km/s. This is rather larger than the experimental values shown in figure 3. However, the conditions of the simulation are also different from the experiment; what is of particular consequence for theoretical estimates is that the electron temperature is taken as poloidally uniform in the simulation, whereas it is the temperature at the blob end (control surface, or divertor plate) that enters the theoretical estimate used in the C-Mod discussion of section 4. The characteristic blob size is also about a factor of two different. From our estimate in equation (14) with

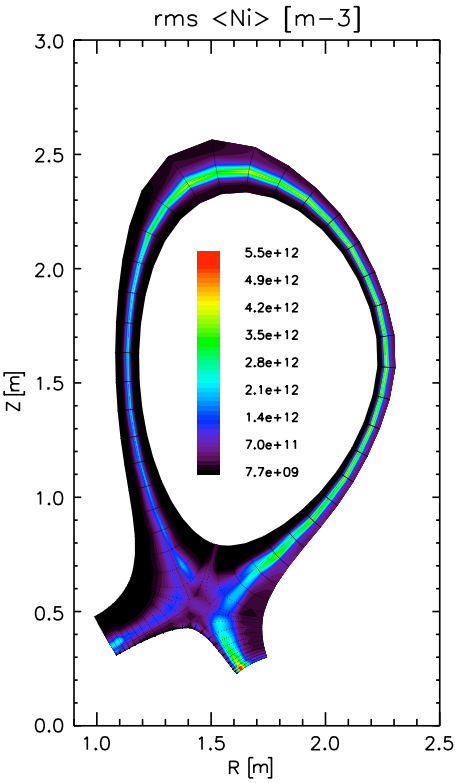

Figure 10. Distribution of rms $\langle N_\mathrm{i}\rangle$ fluctuations at saturation for DIII-D simulation.

blob radius $a \sim 0.5\,\mathrm{cm}$ and $T_\mathrm{e} \sim 20\,\mathrm{eV}$, we obtain $\dot{R} \sim 2.6\,\mathrm{m\,s^{-1}}$, in general agreement with the simulation. The distinction between simulation parameters and experimental parameters may also provide some clues regarding the apparent discrepancy in correlation times noted above.

In a separate series of BOUT simulations a study of plasma turbulence in divertor leg region is conducted. The basic magnetic geometry is based on a DIII-D magnetic reconstruction. The background plasma is modeled approximating typical DIII-D experimental edge data with a set of simulated axisymmetric profiles [25].

Fluctuations exist not only at the outer midplane but in divertor legs as well, see figure (10), which shows results for saturated turbulence. However the leg turbulence appears to be uncoupled from the upstream turbulence as shown in the cross-correlation analysis.

If the reference location is taken at the outer midplane then large values of the cross-correlation function correspond to locations between the lower X-point and the upper virtual X-point, see figure 11(*a*). That was discussed previously in [25, 26]. If, however, the reference location is in the outer leg then large values of the cross-correlation function correspond to locations within the leg itself, see figure 11(*b*). This analysis shows that turbulence upstream and turbulence in the legs are uncoupled. We attribute this decorrelation to the strong shearing of magnetic field near the X-point discussed in preceding sections. It is noteworthy that fluctuations in the divertor legs are observed in both the linear (not shown) and nonlinear (shown) phases; hence we can attribute the divertor-leg turbulence to instabilities in the divertor leg, as discussed in section 3.

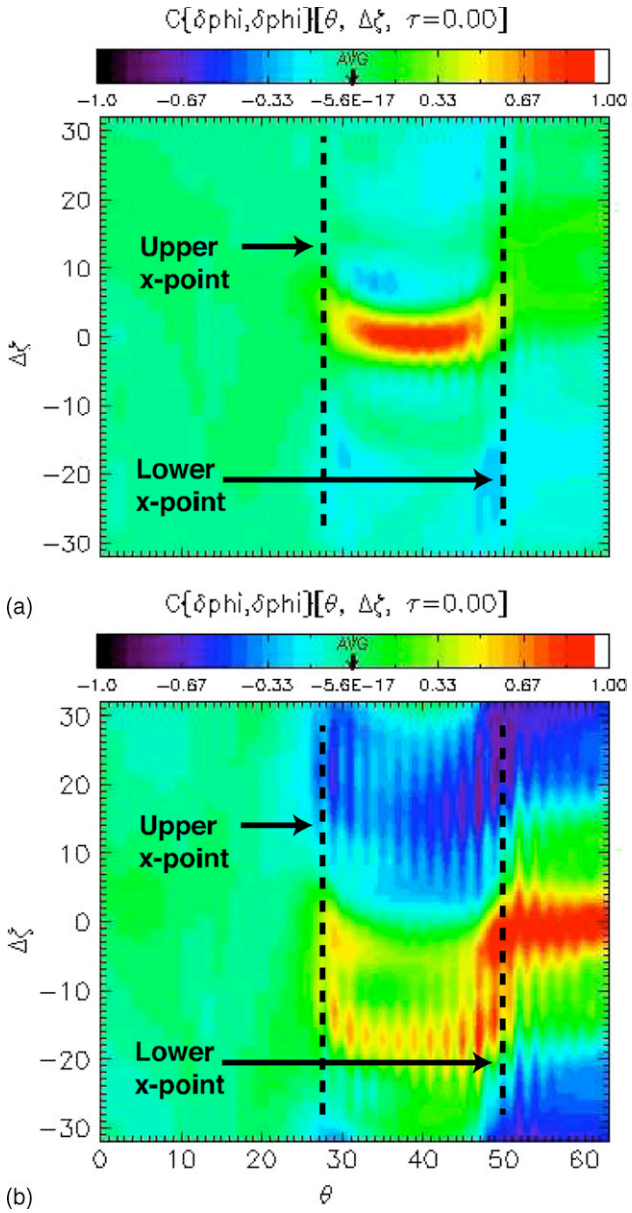

Figure 11. Cross-correlation of fluctuations (for $\tau = 0$) in divertor leg turbulence simulations: (*a*) reference location at outer midplane and (*b*) reference location in outer divertor leg.

6. Conclusion

From the studies presented here, we can draw the following conclusions. (1) The 'heuristic boundary condition' previously developed to describe resistive closure of currents resulting from X-point shear is straightforwardly extended to simultaneously include polarization and viscous (as well as resistive) channels for current closure. (2) Curvature- and sheath-driven instabilities can exist in the private- as well as common-flux regions of divertor legs, isolated from the main SOL; these offer the possibility of broadening the SOL without impacting the main plasma. Divertor-plate tilt can significantly increase the growth rate. Nonlinearly these can develop into divertor-leg blobs. (3) X-point effects can isolate blobs in the main SOL from divertor legs, and non-symmetric blobs in contact with material surfaces can be dominated by sheath-impedance drive. As a main-SOL blob propagates outwards, the region where X-point current closure occurs (the location of the 'control surface') recedes down the divertor leg, but the propagating blob maintains contact with this region, and so propagates as a speed determined by X-point termination, until the control surface reaches a material surface. The blob propagation rate then transitions to the (lower) speed determined by contact with material walls. These results are consistent with the magnitude and relative constancy of C-Mod blob velocities reported in [9]. The X-point effects would be expected to have an impact only at the left-most data point in figure 3. (4) Analytic results are qualitatively confirmed by BOUT fluid simulations. Simulations of C-MOD find blob-like structures with amplitudes and spatial correlation lengths comparable to those observed experimentally. BOUT simulations also provide evidence of instability and fluctuations in divertor legs that is uncorrelated with activity in the main SOL.

Acknowledgment

This work was performed for the US Department of Energy under contracts W7405-ENG-48 at U.C. LLNL and DE-AC02-76CHO3073 at PPPL and Cooperative Agreement DE-FC02-99-ER54512 at MIT.

Appendix. Basic equations for divertor-leg instabilities

We assume that unperturbed plasma parameters do not vary along the field lines. Because of the toroidal symmetry of the unperturbed plasma, this means that the variation occurs only in the direction normal to the flux surfaces. To avoid excessively long equations, we assume that the only quantity that varies in the normal direction is the electron temperature T_e. This assumption can also be justified by the observation that the radial scale-length of T_e in the vicinity of the separatrix is usually shorter than that of the plasma density and ion temperature; also, as it turns out in the subsequent analysis, the instability drive associated with the electron temperature gradient contains a significant numerical multiplier ~3–4.

The perturbations that are most unstable have a ballooning nature, with a slow variation along the field lines; in a number of cases they become essentially pure flute perturbations. For strong magnetic shear near the X-point, the perturbations in the inner and outer divertor legs are uncoupled from each other; similarly, if we consider the common flux region, we assume that perturbations are decoupled from the main SOL [1]. As shown in [2] and section 2 of this paper, the presence of the X-point is folded into the analysis by introducing a boundary condition set on some 'control' surface situated somewhat below the X-point. In this way, we come to the simplified geometry shown in figure 1. In this geometry, our earlier assumption that the unperturbed plasma parameters are constant along the field lines means that these parameters vary only in the x direction, so that the perturbations can be represented as $f(x)\exp(-\mathrm{i}\omega t + \mathrm{i}K_y y + \mathrm{i}K_z z)$. Following [27, 28], we represent the two-dimensional (2D) vector $\boldsymbol{K}$ in the form

$$K_y = k_y + q, \qquad K_z = k_z, \tag{A.1}$$

with k_y defined as

$$k_y = -k_z B_z / B_y. \tag{A.2}$$

In other words, the perturbation becomes $f(x)\exp(iqy)\exp(-i\omega t + i\boldsymbol{k}\cdot\boldsymbol{r})$, with the 2D vector $\boldsymbol{k}$ being perpendicular to the magnetic field. The factor $\exp(iqy)$ describes (a slow) variation of perturbations along the field line, whereas the factor $\exp(i\mathbf{k}\cdot\mathbf{r})$ does not vary along the field line due to condition $\boldsymbol{k}\cdot\boldsymbol{B} = 0$, equation (A.2).

We assume that the poloidal magnetic field in figure 1 is directed towards the divertor plate, and that the toroidal component is directed towards the viewer. In other words, we assume that $B_y \equiv -B_\mathrm{p} < 0$, and that $B_z \equiv B_\mathrm{t} > 0$, with both

$$B_\mathrm{p} > 0, \qquad B_\mathrm{t} > 0. \tag{A.3}$$

We will be using the eikonal approximation, assuming that perturbation length-scale in the x direction is much less than the thickness Δ of the SOL plasma. We will also assume that the x-component of the wavenumber is small compared with k, i.e. $k_x \ll k$. This assumption is based on the results of the earlier works [2, 27, 28], which showed that usually the fastest-growing perturbations are of this type. The other natural assumption is that the poloidal (y) component with the magnetic field is small compared with the toroidal component: this is certainly true in a divertor with not very long legs, where the poloidal distance from the plate to the X-point is significantly smaller than the plasma radius a. We will retain only the lowest-order terms in the parameters

$$k_x/k \ll 1, \qquad B_\mathrm{p}/B_\mathrm{t} \ll 1. \tag{A.4}$$

The second of these inequalities, when combined with condition (A.2), shows also that

$$k_z \ll k_y. \tag{A.5}$$

As the plasma is in contact with the equipotential surface of the divertor plate, the variation of the electron temperature leads to the variation of the unperturbed plasma potential (as the sheath potential scales as T_e [29]), and, accordingly, to the $\boldsymbol{E}\times\boldsymbol{B}$ drift in the unperturbed state. The drift causes the Doppler shift of the perturbation frequency in the (local) plasma rest-frame from Ω to

$$\Omega = \omega - \boldsymbol{k}\cdot\boldsymbol{v}_\mathrm{D}. \tag{A.6}$$

One can check *a posteriori* that the frequency shift caused by the parallel plasma flow is negligible because of the smallness of q.

The instability that we find has an e-folding time much shorter than the ion transit time from the control surface to the divertor plate. Therefore, the ion thermal spread is unimportant; it is also unimportant whether the ion mean free path is shorter or longer than the connection length $L_\parallel$ between the control surface and the divertor plane: the ions enter the problem just via their cross-field inertia. With regard to electrons, we assume that their collision frequency is higher than the growth rate. Under such conditions, the momentum equation can be written as

$$-\Omega^2 m_\mathrm{i} n\boldsymbol{\xi} = -\nabla\delta p + \frac{\delta\boldsymbol{j}_\perp\times\boldsymbol{B}}{c}. \tag{A.7}$$

Here $\boldsymbol{\xi}$ is the displacement vector of a plasma element, related to the velocity perturbation by

$$\delta\boldsymbol{v} = -i\Omega\boldsymbol{\xi}. \tag{A.8}$$

The pressure perturbation in equation (A.7) can be found from the electron thermal balance equation, which yields:

$$\delta p = -nT_\mathrm{e}'\xi_x. \tag{A.9}$$

We have used the fact that the perturbations are essentially divergence-free and that the only unperturbed quantity that depends on x is T_e. The prime here and below means differentiation with respect to x.

One can find the perpendicular current perturbation from equation (A.7):

$$\delta\boldsymbol{j}_\perp = \frac{c}{B^2}\left\{-\Omega^2 m_\mathrm{i} n\left[\boldsymbol{B}\times\boldsymbol{\xi}\right] + \left[\boldsymbol{B}\times\nabla\delta p\right]\right\}. \tag{A.10}$$

To find the perturbation of the parallel current, one has to take the divergence of equation (A.10) and use the current-continuity equation, which yields

$$i\frac{B_\mathrm{p}}{B_\mathrm{t}}q\delta j_\parallel = -\nabla\cdot\delta\boldsymbol{j}_\perp = -\frac{ic\Omega^2 m_\mathrm{i} n}{B^2}\boldsymbol{k}\cdot\left[\boldsymbol{B}\times\boldsymbol{\xi}\right] + \frac{2ic\delta p}{B^3}\boldsymbol{k}\cdot\left[\boldsymbol{B}\times\nabla B\right]. \tag{A.11}$$

Here we have taken into account the fact that, at the edge, the magnetic field is close to the vacuum field and, therefore, $|\nabla\times\boldsymbol{B}| \ll |\nabla B|$. The last term in equation (A.11) describes the curvature drive. Note also that the current-continuity equation shows that $|\delta j_\parallel| \gg |\delta\boldsymbol{j}_\perp|$ (because of the large parallel wavelength of perturbations).

Using inequalities (A.4), (A.5), one finds, to the lowest order,

$$i\frac{B_\mathrm{p}}{B_\mathrm{t}}q\delta j_\parallel = -\frac{ik_y c\Omega^2 m_\mathrm{i} n\xi_x}{B_\mathrm{t}} + \frac{2ick_y\delta p)(\nabla B)_x}{B_\mathrm{t}^2} \tag{A.12}$$

The divertor legs typically form a 45° angle with the horizontal plane; as $\nabla B \approx -\boldsymbol{e}_R B_\mathrm{t}/R$, where $\boldsymbol{e}_R$ is the unit vector in the direction of the major radius R, one has $(\nabla B)_x \approx -B_\mathrm{t}/2^{1/2}R$. Using equation (A.4), one finally obtains

$$i\frac{B_\mathrm{p}}{B_\mathrm{t}}q\delta j_\parallel = -ik_y nc\xi_x\left(\frac{\Omega^2 m_\mathrm{i}}{B_\mathrm{t}} + \frac{2^{1/2}T_\mathrm{e}'}{B_\mathrm{t}R}\right). \tag{A.13}$$

In the case where the plasma is limited at both ends by non-conducting plates (so that at these surfaces $\delta j_\parallel = 0$), and displacement ξ_x is constant along the field line, this equation yields a dispersion relation for the flute instability, $\Omega^2 = -2^{1/2}T_\mathrm{e}'/m_\mathrm{i}R$. In our case, however, the limiting surfaces are conducting, and the situation becomes more complex.

Consider now the parallel structure of perturbations. To do that, we use Maxwell equations and the Ohms law:

$$\nabla\times\delta\boldsymbol{B} = \frac{4\pi}{c}\delta\boldsymbol{j}, \tag{A.14}$$

$$\nabla\times\delta\boldsymbol{E} = \frac{i\Omega}{c}\delta\boldsymbol{B}, \tag{A.15}$$

$$\delta\boldsymbol{E} = i\Omega\frac{\boldsymbol{\xi}\times\boldsymbol{B}}{c} + \eta\boldsymbol{b}\left(\boldsymbol{b}\cdot\delta\boldsymbol{j}\right), \tag{A.16}$$

where $\boldsymbol{b} = \boldsymbol{B}/B$, and η is the parallel resistivity: based on the observation that $|\delta j_\parallel| \gg |\delta \boldsymbol{j}_\perp|$, we retained only the parallel component of the current in the Ohms law. From equations (A.14) and (A.16) one finds:

$$\delta \boldsymbol{E} = \mathrm{i}\Omega \frac{\boldsymbol{\xi} \times \boldsymbol{B}}{c} + \frac{\eta c \boldsymbol{b}}{4\pi} (\boldsymbol{b} \cdot \nabla \times \delta \boldsymbol{B}) . \tag{A.17}$$

Substituting this result into equation (A.15), one obtains

$$\delta B_x = -\mathrm{i} B_\mathrm{p} q \xi_x - \mathrm{i} D_\mathrm{M} k_y^2 \delta B_x / \Omega, \tag{A.18}$$

where

$$D_\mathrm{M} = \eta c^2 / 4\pi \tag{A.19}$$

is the magnetic diffusivity. In other words,

$$\delta B_x = \frac{-\mathrm{i} B_\mathrm{p} q \xi_x}{1 + \mathrm{i} \dfrac{D_\mathrm{m} k_y^2}{\Omega}} . \tag{A.20}$$

Using

$$\mathrm{i} k \delta B_x = 4\pi \delta j_\parallel / c \tag{A.21}$$

and equation (A.10) we then find

$$\Omega^2 = \frac{q^2 v_\mathrm{A}^2 B_\mathrm{p}^2}{B^2 \left(1 + \mathrm{i} \dfrac{D_\mathrm{m} k_y^2}{\Omega}\right)} - \frac{2^{1/2} T_\mathrm{e}'}{R m_\mathrm{i}} . \tag{A.22}$$

We have used here inequalities (A.4) and (A.5). We have also assumed that, in the Ohm's law, the parallel electron inertia can be neglected. This requires that the wavenumber be smaller than ω_pe/c (note that in [28] this condition is written 'upside-down').

When considered as an equation for q, equation (A.22) has two roots, $q_\pm$:

$$q_\pm = \pm q_0;$$

$$q_0 \equiv \frac{B_\mathrm{t}}{B_\mathrm{p} v_\mathrm{A}} \left[\left(1 + \mathrm{i} \frac{D_\mathrm{m} k_y^2}{\Omega}\right) \left(\Omega^2 + \frac{2^{1/2} T_\mathrm{e}'}{R m_\mathrm{i}}\right) \right] . \tag{A.23}$$

This shows that the spatial structure of the perturbation in the poloidal direction is

$$\begin{aligned} \xi_x &= A \exp(\mathrm{i} q_+ y) + B \exp(\mathrm{i} q_- y) \\ &= A \exp(\mathrm{i} q_0 y) + B \exp(-\mathrm{i} q_0 y), \end{aligned} \tag{A.24}$$

where A and B are arbitrary constants. By imposing boundary conditions at the divertor plate and the control surface, and imposing the solvability condition, one can eliminate A and B and obtain the linear dispersion relation.

For the case of perfect line-tying at both ends, for which $q = \pi/\ell_\mathrm{d}$, where

$$\ell_\mathrm{d} = L_\parallel (B_\mathrm{p}/B_\mathrm{t}) \tag{A.25}$$

is the distance between the divertor plate and control surface (figure 1), equation (A.22) describes various regimes of a curvature-driven instability. In particular, if the plasma is perfectly conducting, we recover a standard ballooning instability for sufficiently small magnetic field (sufficiently high plasma β); at higher field (lower β), the instability is stabilized. If, on the other hand, the resistivity is high enough, the first term is significantly reduced (D_M is large), and the instability is recovered even at low betas: this is the resistive-ballooning mode. One can write down the corresponding criteria and see that, for the case of the C-Mod private-flux region, β is too small to make the system unstable for perfect line-tying. However, we will see below that accounting for more realistic boundary conditions at the divertor plate and control surface makes the system strongly unstable.

The boundary conditions can be cast in the form of conditions on the current flowing through the two limiting surfaces. For the solution of the form (A.24), the expressions for the parallel and perpendicular currents, to significant leading order in the small parameters B_p/B_t, k_z/k_y and k_x/k_y is (see equations (A.4) and (A.5)):

$$\begin{aligned} \delta j_\parallel = &-\frac{k_y}{q_0} \left(\frac{c m_\mathrm{i} n \Omega^2}{B_\mathrm{p}} + \frac{2^{1/2} c n T_\mathrm{e}'}{R B_\mathrm{p}} \right) \\ &\times \left[A \exp(\mathrm{i} q_0 y) - B \exp(-\mathrm{i} q_0 y) \right] , \end{aligned} \tag{A.26}$$

$$\begin{aligned} \delta \boldsymbol{j}_\perp = &\frac{c \Omega B_\mathrm{t}}{B^2 k_y} \left(\Omega m_\mathrm{i} n \mathbf{k} + \frac{\mathrm{i} n T_\mathrm{e}' k_y}{\Omega B_\mathrm{t}} \mathbf{K} \times \mathbf{B} \right) \\ &\times \left[A \exp(\mathrm{i} q_0 y) + B \exp(-\mathrm{i} q_0 y) \right] . \end{aligned} \tag{A.27}$$

The component of the plasma current normal to the end surface is (also to the lowest required order in small parameters):

$$\begin{aligned} \delta j_n \big|_{y=0} &= \cos\alpha \frac{B_\mathrm{p}}{B_\mathrm{t}} \delta j_\parallel + \sin\alpha \left(\delta \boldsymbol{j}_\perp\right)_x \\ &= -\frac{c n k_y \cos\alpha}{q_0 B_\mathrm{t}} \left(m_\mathrm{i} \Omega^2 + \frac{2^{1/2} T_\mathrm{e}'}{R} \right) (A - B) \\ &\quad + \frac{\mathrm{i} c k_y n T_\mathrm{e}' \sin\alpha}{B_t} (A + B) . \end{aligned} \tag{A.28}$$

$$\begin{aligned} \delta j_n \big|_{y=\ell_\mathrm{d}} = \frac{B_\mathrm{p}}{B_\mathrm{t}} \delta j_\parallel + \left(\delta \boldsymbol{j}_\perp\right)_y = -\frac{c n k_y}{q_0 B_\mathrm{t}} \left(m_\mathrm{i} \Omega^2 + \frac{2^{1/2} T_\mathrm{e}'}{R} \right) \\ \times \left[A \exp(\mathrm{i} q_0 \ell_\mathrm{d}) - B \exp(-\mathrm{i} q_0 \ell_\mathrm{d}) \right] \end{aligned} \tag{A.29}$$

We assume that the length of the divertor leg is not too small, namely that $k_y \ell_\mathrm{d} > B_\mathrm{t}/B_\mathrm{p}, \tan\alpha$.

We now match these currents to the currents flowing through the sheath (at $y = 0$) and the current flowing to the X-point region (at $y = \ell_\mathrm{d}$). To find these currents, we have to find the potential perturbations near these surfaces. Proceeding as in [28], we find that

$$\delta\phi = \frac{\Omega B_\mathrm{t}}{c k_y} (A + B) \tag{A.30}$$

near the lower boundary and

$$\delta\phi = \frac{\Omega B_\mathrm{t}}{c k_y} (A \exp(\mathrm{i} q_0 \ell_\mathrm{d}) + B \exp(-\mathrm{i} q_0 \ell_\mathrm{d})) \tag{A.31}$$

near the upper boundary.

Using the boundary conditions relating the currents and potential perturbations, one can obtain the dispersion relation. At the lower boundary ($y = 0$) we have from the sheath CVC (cf equation (33) of [28]):

$$\begin{aligned} \delta j_n \big|_{y=0} = -en(A + B) \left\{ u \frac{B_\mathrm{p}}{B_\mathrm{t}} \cos\alpha \left[\left(\Lambda + \frac{1}{2}\right) \frac{T_\mathrm{e}'}{T_\mathrm{e}} + \frac{e \Omega B_\mathrm{t}}{c T_\mathrm{e} k_y} \right] \right. \\ \left. + \mathrm{i}\Omega \sin\alpha \right\} \end{aligned} \tag{A.32}$$

The parameter Λ is the logarithm of $(2\pi)^{-1/2}$ times the ratio of electron thermal velocity to the ion thermal velocity and is typically ~3–3.5. So, there is a significant numerical factor in front of T_e'. As mentioned at the beginning of the appendix, this makes the T_e' drive more important than the drive associated with, say, T_i'. From equations (A.28) and (A.32), we obtain the following equation:

$$\frac{ck_y\cos\alpha}{q_0 B_t}\left(m_i\Omega^2+\frac{2^{1/2}T_e'}{R}\right)(A-B) = -e(A+B)\left\{u\frac{B_p}{B_t}\cos\alpha\left[\left(\Lambda+\frac{1}{2}\right)\frac{T_e'}{T_e}+\frac{e\Omega B_t}{cT_e k_y}\right] + i\Omega\sin\alpha+\frac{ick_y T_e'\sin\alpha}{eB_t}\right\}. \tag{A.33}$$

At the control surface ($y=\ell_d$), we use the 'heuristic' boundary condition (see section 2) which can be represented as

$$\delta j_n = \frac{B_p}{B_t}\left|k_y\right|\sigma_H\delta\phi \tag{A.34}$$

or, accounting for equations (A.29) and (A.31),

$$\frac{ck_y n}{q_0 B_p}\left(m_i\Omega^2+\frac{2^{1/2}T_e'}{R}\right)(A\exp(iq_0\ell_d - B\exp(-iq_0\ell_d))) = \frac{\left|k_y\right|\sigma_H\Omega B_t}{ck_y}(A\exp(iq_0\ell_d)+B\exp(-iq_0\ell_d)). \tag{A.35}$$

From the solubility condition of the set (A.33), (A.35), one can obtain a dispersion relation which covers, in a unified manner, a number of effects that have been considered previously in a piecemeal manner: the drive, associated with the temperature gradient and sheath BC, the flute instability in the presence of current leaks to the end surfaces, the role of the boundary condition at the control surface, the effect of a tilt of the divertor plate, and possible finite-beta modes. It covers also the effect of resistive ballooning.

We concentrate here on the case of a low-β plasma. We first derive a simplified dispersion relation for this case by taking the limit of $v_A\to\infty$ and then formulate applicability conditions for such an approximation.

In the limit of a large Alfvèn velocity, one has

$$q_0\ell_d \ll 1. \tag{A.36}$$

In this case, it is convenient to introduce, instead of A and B, the coefficients a and b, according to

$$a=\frac{A-B}{q_0},\qquad b=(A+B)\ell_d. \tag{A.37}$$

One then has, for small q_0:

$$\frac{A\exp(iq_0\ell_d)-B\exp(-iq_0\ell_d)}{q_0}\approx a+b;$$
$$A\exp(iq_0\ell_d)-B\exp(-iq_0\ell_d)\ell_d+\approx b/\ell_d, \tag{A.38}$$

so that equations (A.33) and (A.35) are reduced to

$$\frac{ck_y\cos\alpha}{B_t}\left(m_i\Omega^2+\frac{2^{1/2}T_e'}{R}\right)a\ell_d = -eb\left\{u\frac{B_p}{B_t}\cos\alpha\left[\left(\Lambda+\frac{1}{2}\right)\frac{T_e'}{T_e}+\frac{e\Omega B_t}{cT_e k_y}\right]+i\Omega\sin\alpha + \frac{ick_y T_e'\sin\alpha}{eB_t}\right\} \tag{A.39}$$

and

$$\frac{ck_y n}{B_p}\left(m_i\Omega^2+\frac{2^{1/2}T_e'}{R}\right)a\ell_d = b\left[\frac{\left|k_y\right|\sigma_H\Omega B_t}{ck_y}-\frac{ck_y n}{B_p}\left(m_i\Omega^2+\frac{2^{1/2}T_e'}{R}\right)\ell_d\right], \tag{A.40}$$

where from the dispersion relation (7) of the main body of the paper immediately follows, with $\Delta\equiv T_e/\left|T_e'\right|$.

We now formulate conditions under which the flute approximation (A.36) holds. As we are interested in modes whose growth rate is comparable to, or greater than, the growth rate of a curvature-driven mode, i.e. $|\Omega|^2 > T_e'/Rm_i$, one can rewrite the condition (A.36) as:

$$|q_0|\,\ell_d \approx \frac{B_t\ell_d\,|\Omega|}{B_p v_A}\left|1+i\frac{D_M k_y^2}{\Omega}\right|^{1/2}\ll 1. \tag{A.41}$$

If the plasma electrical conductivity is high, so that the second term under the square root is small, the validity of the flute approximation becomes

$$\frac{B_T\ell_d\,|\Omega|}{B_p v_A}\ll 1 \tag{A.42}$$

(Note that in the opposite limiting case, there may exist unstable modes localized near the divertor plate; these modes have been considered in [28]. The general dispersion relation based on equations (A.33), (A.35) allows one to consider various intermediate cases.)

If the electrical conductivity is low, so that

$$D_M k_y^2 \gg |\Omega|, \tag{A.43}$$

the applicability condition of the flute approximation becomes more stringent:

$$\frac{B_t\ell_d}{B_p v_A}\left(|\Omega|\,D_M k_y^2\right)^{1/2}\ll 1. \tag{A.44}$$

If this condition breaks down, the unstable modes localized near the divertor plates by the effect of resistive ballooning may appear.

References

[1] Farina D., Pozzoli R. and Ryutov D.D. 1993 *Nucl. Fusion* **33** 1315

[2] Ryutov D.D. and Cohen R.H. 2004 *Contrib. Plasma Phys.* **44** 168

[3] Russell D.A., D'Ippolito D., Myra J.R., Nevins M. and Xu X.Q. 2004 *Phys. Rev. Lett.* **93** 265001
[4] Myra J.R. and D'Ippolito D.A. 2005 *Phys. Plasmas* **12** 92511
[5] Myra J.R., Russell D.A. and D'Ippolito D.A. 2006 *Phys. Plasmas* **13** 112502
[6] Ryutov D.D., Cohen R.H. and Helander P. 2001 *Plasma Phys. and Controlled Fusion* **43** 1399
[7] Myra J.R., D'Ippolito D.A., Xu X.Q. and Cohen R.H. 2000 *Phys. Plasmas* **7** 2290
[8] Terry J.L. *et al* 2003 *Phys. Plasmas* **10** 1739
[9] Grulke O., Terry J.L, LaBombbard B. and Zweben S.J. 2006 *Phys. Plasmas* **13** 012306
[10] Myra J.R. *et al* 2006 *Phys. Plasmas* **13** 092509
[11] Zweben S.J. *et al* 2006 *Phys. Plasmas* **13** 056114
[12] Krasheninnikov S.I., Ryutov D.D. and Yu G. 2004 *J. Plasma Fusion Res.* **6** 139
[13] Krasheninnikov S.I. 2001 *Phys. Lett.* **A 283** 368
[14] Garcia O.E., Bian N.H. and Fundamenski W. 2006 *Phys. Plamas* **13** 082309
[15] D'Ippolito D.A., Myra J.R. and Krasheninnikov S.I. 2002 *Phys. Plasmas* **9** 222
[16] Cohen R.H. and Ryutov D.D. 2006 *Contrib. Plasma Phys.* **46** 678
[17] Ryutov D.D. 2006 *Phys. Plasmas* **13** 122307
[18] Cohen R.H. and Ryutov D.D. 1996 *Contrib. Plasma Phys.* **36** 161
[19] Cohen R.H. and Ryutov D.D. 1997 *Nucl. Fusion* **37** 621
[20] Kotschenreuther M. 2006 private communication (University of Texas)
[21] Berk H.L., Ryutov D.D. and Tsidulko Yu A. 1993 *Phys. Fluids* B **3** 1346
[22] Berk H.L., Cohen R.H., Ryutov D.D., Tsidulko Yu A. and Xu X.Q. 1993 *Nucl. Fusion* **33** 263
[23] Counsell G. 2006 private communication (Culham Science Centre)
[24] Xu X.Q., Cohen R.H., Rognlien T.D. and Myra J.R. 2000 *Phys. Plasmas* **7** 1951
[25] Umansky M.V. *et al* 2004 *Contrib. Plasma Phys.* **44** 182
[26] Umansky M.V., Rognlien T.D. and Xu X.Q. 2005 *J. Nucl. Mater.* **337–339** 266
[27] Farina D., Pozzoli R. and Ryutov D. 1993 *Plasma Phys. Control. Fusion* **35** 1271
[28] Cohen R.H. and Ryutov D.D. 2005 *Plasma Phys. Control. Fusion* **47** 1187
[29] Stangeby P. 2000 *The Plasma Boundary of Magnetic-Fusion Devices* (Bristol, UK: Institute of Physics Publishing)